

1 **From salinity to nanoplastics: redefining safe yield in strip-island**

2 **aquifers under emerging contaminant threats**

3 **Tianyuan Zheng^{1,2,3*}, Chunxiang Ma^{1,2,3}, Shaobo Gao^{1,2,3**}, Jian Luo⁴**

4 ¹ College of Environmental Science and Engineering, Ocean University of China,

5 Qingdao, China, Qingdao 266100, China.

6 ² Key Laboratory of Marine Environment and Ecology, Ministry of Education, Ocean

7 University of China, Qingdao 266100, China.

8 ³ Shandong Provincial Key Laboratory of Marine Engineering Geology and the

9 Environment, Ocean University of China, Qingdao 266100, China.

10 ⁴ School of Civil and Environmental Engineering, Georgia Institute of Technology,

11 Atlanta, GA 30332, USA.

12 Corresponding authors: Tianyuan Zheng (zhengtianyuan@ouc.edu.cn);

13 Shaobo Gao (gaoshaobo@ouc.edu.cn)

14

15 **Abstract:** Nanoplastic contamination is emerging as a significant threat to
16 groundwater security on small islands, where freshwater lenses serve as primary
17 water supplies. Existing groundwater management frameworks are largely based on
18 salinity intrusion and do not account for the distinct transport behavior of nanoplastics.
19 This study formulates a multi-physics numerical model incorporating variable-density
20 groundwater flow, salt transport, and nanoplastic migration processes to investigate
21 nanoplastic transport in idealized strip-island aquifers under pumping conditions. The
22 model is calibrated using laboratory-scale data and evaluated at the field scale.
23 Results show that nanoplastic migration is controlled not only by advection –
24 dispersion processes but also by particle-specific interactions, leading to transport
25 dynamics fundamentally different from those of dissolved salts. In particular, the
26 higher effective dispersivity of nanoplastics causes earlier breakthrough at extraction
27 wells and the formation of broader contaminant transition zones. Pronounced scale
28 effects are observed: while laboratory simulations exhibit rapid upward coning and
29 contamination, field-scale simulations indicate attenuated coning and stabilization
30 over substantially longer timeframes. Sensitivity analysis identifies nanoplastic
31 dispersivity as the dominant parameter influencing well contamination risk. These
32 findings demonstrate that safe extraction strategies based solely on salinity thresholds
33 may underestimate contamination risks and that well placement and pumping design
34 must account for nanoplastic transition zones. The study provides a process-based
35 framework for adapting groundwater management to emerging nanoplastic pollution
36 in vulnerable island environments.

37 **Keywords:** Groundwater lens; Seawater intrusion; Groundwater contamination;

38 Pumping optimization

39

40 **1. Introduction**

41 Islands host nearly 10% of the global population and cover approximately 6.7%
42 of the Earth’s terrestrial surface (Sayre et al., 2019). On many small islands, limited
43 surface water availability makes groundwater a critical resource for local communities
44 (Dose et al., 2014). Notably, numerous Pacific islands rely on shallow freshwater
45 lenses—buoyant bodies of freshwater overlying saltwater in highly permeable
46 aquifers—as their primary water supply (Sharan et al., 2021; White and Falkland,
47 2010). The formation, stability, and morphology of these lenses result from the
48 interplay between density contrasts and multiple external factors, including climate,
49 geological structures, and anthropogenic activities such as groundwater pumping and
50 subsurface barrier installation (Alsumaiei and Bailey, 2018; Ketabchi et al., 2014;
51 Tang et al., 2021, 2022; Yan et al., 2021; Yang et al., 2025; Gao et al., 2025; Zheng et
52 al., 2025). Excessive pumping readily induces saline upconing, degrades water quality,
53 and threatens long-term water security (Abdoulhalik and Ahmed, 2018; Dagan and
54 Bear, 1968; Houben and Post, 2017; Werner et al., 2009).

55 Beyond salinity intrusion, nanoplastic contamination has emerged as an
56 additional and largely unaddressed threat to island groundwater systems.
57 Microplastics are pervasive environmental pollutants detected in marine environments,
58 soils, and groundwater worldwide (Koelmans et al., 2022; Koutnik et al., 2021; Li et
59 al., 2018; Ren et al., 2021; Thompson et al., 2024). Oceanic concentrations continue
60 to rise due to plastic persistence and ongoing inputs (Isobe et al., 2019). Nanoplastics,
61 which are generated through the fragmentation of larger plastic debris and
62 microplastics, may occur at even higher particle-number concentrations, with coastal
63 waters often exhibiting higher levels than open-ocean regions (ten Hietbrink et al.,
64 2025). Emerging evidence indicates that seawater intrusion facilitates the transport of
65 microplastics into coastal aquifer systems (Chen et al., 2024a). Because island
66 aquifers are completely surrounded by seawater, freshwater lenses are particularly
67 vulnerable to marine-sourced nanoplastic contamination (Fig. 1).

68 The maximum safe extraction rate for freshwater lenses is typically estimated

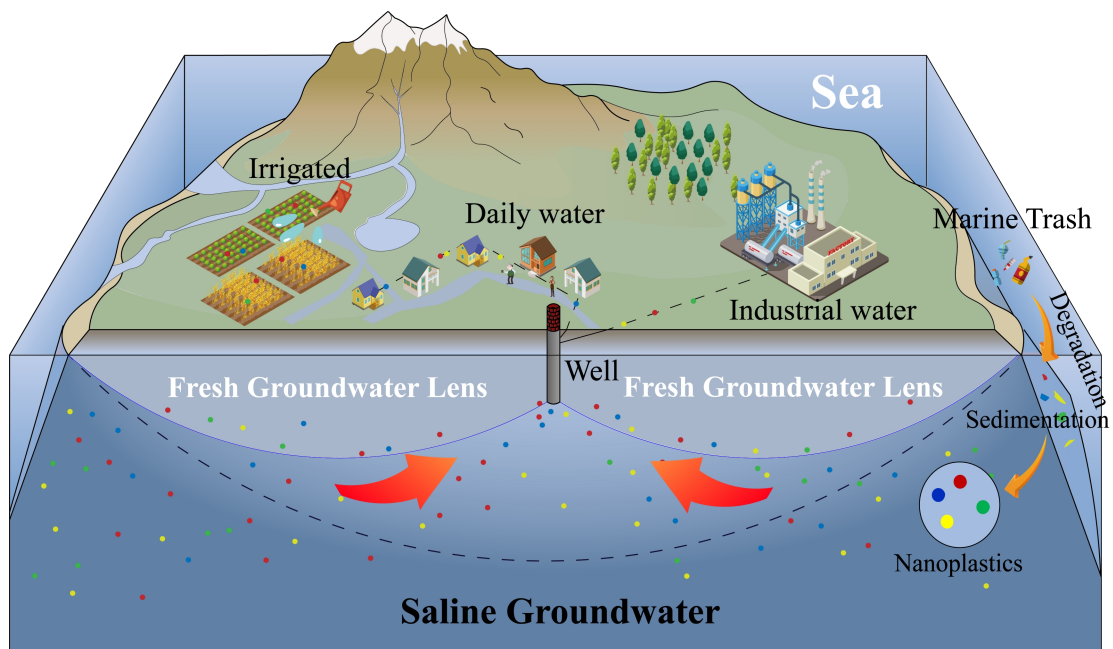
69 using analytical solutions that assume a sharp interface between freshwater and
70 seawater (Muskat, 1938). Such approaches are widely used in two-dimensional
71 strip-island models to determine the pumping threshold at which the saline interface
72 reaches the well screen (Tang et al., 2020, 2021, 2024). While computationally
73 efficient, these models neglect hydrodynamic dispersion and the development of a
74 brackish transition zone, which can be extensive in highly permeable island aquifers
75 (Coulon et al., 2022; Babu et al., 2020). Consequently, current safe-yield assessments
76 often overlook realistic mixing processes and contaminant transport within the
77 transition zone, potentially underestimating water-quality risks.

78 Transport processes of nanoplastics in porous media differ fundamentally from
79 those of dissolved solutes. Early modeling efforts adapted classical
80 advection-dispersion equations with simple adsorption terms (Babakhani et al., 2017),
81 but subsequent studies have demonstrated that the migration of microplastics and
82 nanoplastics involves additional mechanisms such as adsorption-desorption, clogging,
83 interception, and aggregation (Liu et al., 2025; Yuan et al., 2024). Importantly,
84 nanoplastic dispersion coefficients depend on particle size and flow velocity (Wang
85 and Sedighi, 2023). Under pumping conditions that induce upward coning flow fields,
86 these properties suggest that nanoplastics may migrate toward extraction wells more
87 rapidly than dissolved salts and form a broader or earlier contaminant transition zone
88 (Wang and Sedighi, 2023; Alkindi et al., 2011; Lee et al., 2017). Traditional
89 sharp-interface and salinity-based intrusion models fail to capture this behavior, which
90 has remained largely unexplored in island freshwater lens studies.

91 Taken together, there are two critical gaps that are interdependent and
92 collectively undermine reliable groundwater management. First, existing safe-yield
93 models oversimplify the freshwater-seawater transition zone by neglecting
94 dispersion-driven mixing. This oversimplification is further exacerbated when
95 combined with the poorly characterized transport of nanoplastics, which exhibit
96 unique migration dynamics that cannot be captured by traditional solute models.
97 Second, the distinct migration behavior of nanoplastics under pumping-induced

98 coning remains poorly understood. Current modeling frameworks, largely derived
99 from solute transport theory, do not adequately capture transient nanoplastic
100 breakthrough or particle-specific transport dynamics.

101 To address these gaps, this study develops a coupled numerical model that
102 integrates variable-density groundwater flow, salt transport, and nanoplastic migration
103 in island aquifers. This study aims to: (1) quantify marine-derived nanoplastic
104 accumulation in freshwater extraction wells under pumping conditions; (2) assess how
105 nanoplastic transport, especially enhanced dispersivity, alters the maximum safe
106 extraction rate compared to traditional salinity-based thresholds; and (3) evaluate the
107 sensitivity of nanoplastic migration and associated risks to key hydrogeological
108 parameters and operational factors. By incorporating nanoplastic transport parameters
109 derived from laboratory column experiments and conducting simulations at both
110 laboratory and field scales, this work provides critical insights for adjusting
111 groundwater management strategies to safeguard island freshwater resources in the
112 face of emerging nanoplastic pollution.



113
114 Fig. 1. Schematic diagram of freshwater lenses and nanoplastic contaminant
115 distribution in an idealized strip-island aquifer under groundwater extraction.

116 **2. Methods**

117 **2.1 Mathematical model**

118 To simplify the problem and enhance computational tractability, the following
119 key assumptions are adopted based on established modeling practices in coastal
120 aquifer studies (Stoeckl and Houben, 2012; Yao et al., 2019): (i) the aquifer is
121 homogeneous and isotropic; (ii) fluid density depends solely on groundwater salinity,
122 with thermal effects considered negligible; (iii) the density of nanoplastic particles is
123 assumed to be approximately equal to that of water, which is representative of
124 neutrally buoyant or aged nanoplastic particles; (iv) the saturated zone is initially
125 saturated with seawater, and rainfall infiltration is spatially uniform and temporally
126 constant; (v) groundwater flow is simulated within a two-dimensional vertical profile
127 of the strip island, leveraging the geometric symmetry of the idealized domain; and
128 (vi) tidal influences are neglected, and constant head boundary conditions are imposed
129 at the seawater interface.

130 This study presents an integrated numerical framework that extends a
131 variable-density groundwater flow model for the unsaturated-saturated zone by
132 incorporating salinity and nanoplastic transport modules. The nanoplastic transport
133 model combines advective–dispersive transport with nanoplastic adsorption
134 mechanisms. The resulting framework simultaneously simulates variable-density
135 groundwater flow, dissolved salt transport, and nanoplastic migration via coupled
136 advection-dispersion and adsorption processes. Governing equations for the
137 variable-density flow and salinity transport components are available in Text S1.

138 Research suggests that nanoplastic transport is primarily influenced by particle
139 movement and physical/physicochemical interactions with porous media surfaces (Al
140 Harraq and Bharti, 2022; Ranjan et al., 2023; Ren et al., 2022; Waldschläger and
141 Schüttrumpf, 2020). Particle movement is described in the equations as advection,
142 diffusion and dispersion effects, while physicochemical interactions with porous
143 media are characterized by mechanisms such as adhesion and detachment, straining
144 on aggregates and individual particles, blockage, and maturation. The subsurface

145 transport of nanoplastic particles is governed by an advection-dispersion equation, a
 146 framework established for nanoplastic migration that captures advection, dispersion,
 147 and adsorption processes (Liu et al., 2025):

$$\frac{\partial}{\partial t}(S_w \theta C_{np}) + \frac{\partial}{\partial t}(\rho_b s) + \nabla C_{np} \frac{k_r \mathbf{k}}{\mu} \nabla P + \nabla \cdot [-\theta S_w D_{np} \nabla C_{np}] = f \quad (1)$$

$$\frac{\rho_b \partial s}{\partial t} = \theta K_{att} \psi_b C_{np} e^{-\frac{s}{\lambda}} - \rho_b K_{det} s + \theta \rho_b K_{rip} s C_{np} \quad (2)$$

148 where C_{np} represents the concentration of nanoplastics in groundwater [ML^{-3}], ρ_b
 149 denotes the bulk density of the aquifer medium [ML^{-3}], s is the mass of
 150 nanoplastics attached per unit mass of solid [MM^{-1}], D_{np} is the hydrodynamic
 151 dispersion coefficient of nanoplastics [L^2T^{-1}], and f is the source-sink term
 152 [$ML^{-3}T^{-1}$]. K_{att} is the first-order colloidal attachment coefficient [T^{-1}], parameter λ
 153 represents the strain capacity of porous media [MM^{-1}], K_{det} is the first-order colloidal
 154 detachment coefficient [T^{-1}], and K_{rip} is the ripening kinetic rate coefficient
 155 [$M^{-1}L^3T^{-1}$].

156 The adhesion of nanoplastics in porous media is described by the following
 157 governing equation:

$$\psi_b = \left(1 - \frac{s}{s_{max}}\right) \quad (3)$$

158 where ψ_b denotes the adhesion state of nanoplastics in porous media [-], and s_{max}
 159 represents the maximum mass of nanoplastics that can be retained per unit mass of
 160 porous medium [MM^{-1}].

161 The variation in hydraulic conductivity as a function of porosity is characterized
 162 by the following relationship (Zheng, 2014):

$$\frac{K}{K_0} = \left(\frac{\theta}{\theta_0}\right)^3 \left(\frac{1-\theta_0}{1-\theta}\right)^3 \quad (4)$$

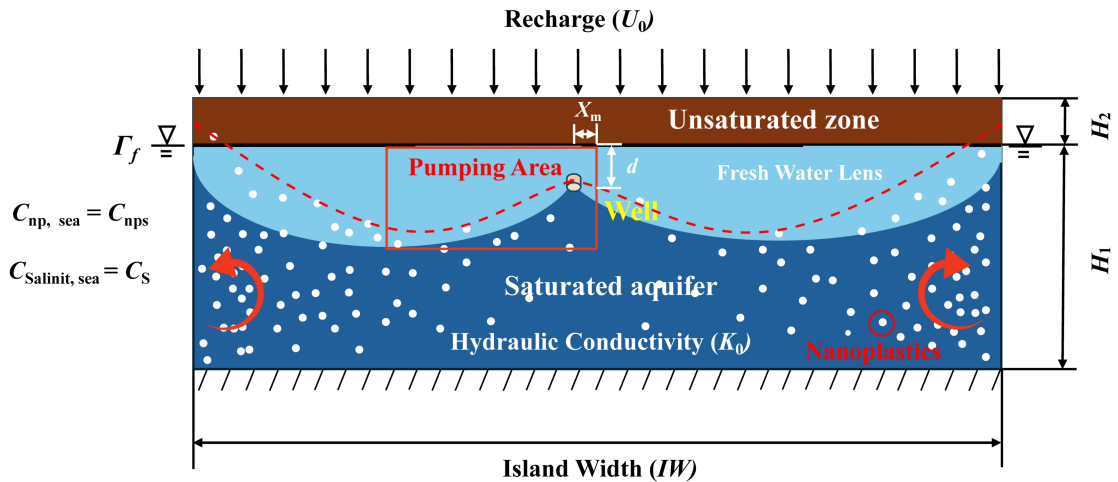
163 where K is the hydraulic conductivity of the porous medium [LT^{-1}], K_0 is the
 164 hydraulic conductivity of the initial porous medium [LT^{-1}], and θ_0 is the porosity of
 165 the initial water-bearing medium [-].

166 The approximate analytical solution derived by Tang et al. (2021) describes the
 167 critical pumping rate preventing brine intrusion when pumping wells are located in
 168 the idealized strip island's central region. The theoretical maximum safe extraction
 169 rate is expressed as:

$$Q_{Tmax} = \omega(W - x_m) - \frac{\delta(1 + \delta)Kd^2}{(W - x_m)} \quad (5)$$

$$\delta = \frac{(\rho_s - \rho_f)}{\rho_f} \quad (6)$$

170 where ω is the infiltration rate at the upper surface of the unsaturated zone [LT^{-1}],
 171 ρ_s is the seawater density [ML^{-3}], ρ_f is the freshwater density [ML^{-3}], d is the
 172 distance from the well to the lower boundary of the unsaturated zone [L], W is the half
 173 width of the idealized strip island [L], x_m is the distance from the well to the centre
 174 of the idealized strip island [L].



175

176 Fig. 2. Conceptual model of nanoplastic pollution in an idealized strip-island aquifer
 177 with central pumping. The model depicts an unsaturated zone (height H_2) over a
 178 saturated zone (height H_1). Freshwater lenses are shown in light blue and saline
 179 groundwater in dark blue. Key parameters include island width (IW), continuous
 180 recharge (U_0), seawater salinity (C_s), and seawater nanoplastic concentration (C_{nps}).

181 2.2 Numerical Solution

182 The numerical simulation investigates the migration behavior of nanoplastics
 183 under pumping conditions in an idealized strip-island aquifer. The laboratory-scale
 184 model domain (60 cm×17 cm) was constructed following the configuration
 185 established by Tang et al. (2021) (Fig. S4), while a field-scale model (600 m×50 m)
 186 was developed to assess field-level transport phenomena. Key simulation parameters
 187 are provided in Table 1. Model parameters calibrated from laboratory-scale
 188 experiments were extrapolated to the field scale assumed for the modeling study to
 189 evaluate the consistency of nanoplastic migration patterns across scales. At the ocean
 190 boundary, a constant head (Dirichlet) condition was imposed with a specified
 191 hydraulic head (H_1) and a salt concentration of 34.7 g/L; tidal influences were
 192 neglected. A constant flux (Neumann) condition was applied to the upper boundary,
 193 representing recharge at a rate U_0 . Fig. 2 shows a vertical cross-section of a typical
 194 freshwater lens in an idealized island under single-well pumping conditions.
 195 Additional aquifer properties are summarized in Table 1.

196 **Table 1.** Numerical Simulation Parameters for Variable-Density Flow and Nanoplastic
 197 Transport (Laboratory and Field Scales)

Parameter	Symbol	Unit	Value
<i>Variable density parameter</i>			
Density of sea water	ρ_0	kg/m ³	1025
Density of freshwater	ρ_f	kg/m ³	1000
Seawater salinity	C_s	mol/L	0.5989

<i>Nanoplastics properties PS-Pd-1</i>			
Constant ^{a, b}	λ	mg/kg	1.6
First-order colloidal attachment coefficient ^{a, b}	K_{att}	1/s	0.0025
Euler number ^a	e	—	2.7183
The maximum solid phase particle concentration ^{a, b}	S_{max}	mg/kg	10
First-order colloidal detachment coefficient ^{a, b}	K_{det}	1/s	0.001
Ripening kinetic rate coefficient ^{a, b}	K_{rip}	m ³ /(g·s)	0.009
Longitudinal dispersivity ^b	$\alpha_{LPS-Pd-1}$	cm	0.91
The average relative molecular weight of nanoplastics ^c	N_m	g/mol	70000

<i>Nanoplastics properties PS-Pd-2</i>			
Constant ^{a, b}	λ	mg/kg	1.7
First-order colloidal attachment coefficient ^{a, b}	K_{att}	1/s	0.0002
The maximum solid phase particle concentration ^{a, b}	S_{max}	mg/kg	10
First-order colloidal detachment coefficient ^{a, b}	K_{det}	1/s	0.005
Ripening kinetic rate coefficient ^{a, b}	K_{rip}	m ³ /(g·s)	0.007
Longitudinal dispersivity ^b	$\alpha_{LPS-Pd-2}$	cm	1.06
The average relative molecular weight of nanoplastics ^c	N_m	g/mol	70000

<i>Laboratory Porous medium properties</i>			
Island width ^d	IW	cm	60
Saturated zone thickness ^d	H_1	cm	15

Unsaturated zone thickness ^d	H_2	cm	2
Rainfall infiltration ^d	U_0	cm/min	0.80
Porosity ^d	θ_0	—	0.38
Longitudinal dispersivity	α_L	cm	0.2
Hydraulic conductivity ^d	K_0	cm/min	200
<i>Field-scale Porous medium properties</i>			
Island width	IW	m	600
Saturated zone thickness	H_1	m	45
Unsaturated zone thickness	H_2	m	5
Rainfall infiltration	U_0	m/s	2×10^{-8}
Porosity	θ_0	—	0.38
Longitudinal dispersivity	α_L	m	0.5
Hydraulic conductivity	K_0	m/s	0.0001

198 a. Data from Liu et al. (2025)

199 b. Data inversion was performed based on the experimental data.

200 c. Data from Singh et al. (2025)

201 d. Experimental water pumping scenario from Tang et al. (2021)

202 The coupled governing equations for variable-density saturated groundwater
203 flow and solute transport were solved numerically via COMSOL Multiphysics, with
204 boundary conditions prescribed accordingly. The system of equations was solved
205 iteratively using a preconditioned conjugate gradient (PCG) method with a relative
206 tolerance of 1×10^{-4} . Initial time steps of 0.001 s and 0.001 d were adopted for the
207 transient analyses.

208 The computational domain for the laboratory-scale model was discretized into
209 63,928 triangular elements and 32,350 nodes, with a maximum element diameter of 2
210 mm. For the field-scale model, the domain was discretized into 30,000 quadrilateral
211 elements and 30,651 nodes, with a maximum element diameter of 1 m. The selected
212 mesh sizes, in conjunction with the hydrodynamic dispersion parameters, conformed

213 to the Péclet number criterion to minimize numerical dispersion and ensure solution
 214 stability (Voss and Provost, 2002):

$$Pe_1 = \frac{v_1 \Delta L_1}{D_1 + \alpha_{L1} v_1} \approx \frac{\Delta L_1}{\alpha_{L1}} = 1 \leq 4 \quad (7)$$

$$Pe_2 = \frac{v_2 \Delta L_2}{D_2 + \alpha_{L2} v_2} \approx \frac{\Delta L_2}{\alpha_{L2}} = 2 \leq 4 \quad (8)$$

215 where Pe_1 is the Péclet number in laboratory-scale [-], Pe_2 is the Péclet number in
 216 field-scale [-], ΔL_1 is the grid length in laboratory-scale [L], ΔL_2 is the grid length
 217 in field-scale [L], v_1 is flow velocity in laboratory-scale [LT^{-1}], v_2 is flow velocity
 218 in field-scale [LT^{-1}], D_1 is diffusion coefficient in laboratory-scale [L^2T^{-1}], D_2 is
 219 diffusion coefficient in field-scale [L^2T^{-1}], α_{L1} is the longitudinal dispersivity in
 220 laboratory-scale [L], α_{L2} is the Longitudinal dispersivity in field-scale [L].

221 Stabilization times for laboratory and field simulations were determined using a
 222 convergence criterion: the system was considered stable when the relative change in
 223 wellhead salinity and nanoplastic concentration was less than 1% over three
 224 consecutive time steps.

225 A continuous rainfall-driven model was developed to simulate freshwater lens
 226 dynamics and well extraction in an idealized island aquifer. The simulation comprises
 227 two distinct hydraulic phases: Phase I involves the formation of a stable freshwater
 228 lens under continuous rainfall infiltration and seawater intrusion; Phase II initiates
 229 groundwater extraction via a single pumping well, leading to the development of a
 230 stable saline upconing zone. In the laboratory-scale setup, the horizontal distance x_m
 231 from the pumping well to the island center was set to 0, 2.5, 5, 7.5, 10, 12.5, 15, 17.5,
 232 and 20 cm. The vertical distance d from the well screen to the base of the saturation
 233 zone was defined as 0, 5, 10, 12, 15, 18, 20, and 25 mm. Hydraulic conductivity K_0
 234 values were assigned as 150, 175, 200, 225, and 250 cm/min, with corresponding

235 recharge rates U_0 of 0.6, 0.7, 0.8, 0.9, and 1.0 cm/min. For the field-scale scenario, the
236 pumping well was positioned at a horizontal distance $x_m=5$ m from the island center,
237 corresponding to a central well location. The hydraulic conductivity K_0 was set to
238 1×10^{-4} m/s, with a recharge rate $U_0 = 2 \times 10^{-8}$ m/s (Tang et al., 2021).

239 **2.3 Evaluation Indicators**

240 Nanoplastic concentrations at the wellhead were monitored to evaluate the
241 impacts of nanoplastics on island freshwater lens development projects. The
242 seawater-freshwater interface of the freshwater lens was designated as 0.347 g/L,
243 corresponding to 1% seawater salinity. Contemporary laboratory investigations
244 typically utilize nanoplastic concentrations ranging from 10 $\mu\text{g/L}$ to 100 mg/L. Owing
245 to constraints associated with nanoplastic preparation protocols and detection
246 capabilities, the migration parameters of nanoplastics in this study were derived under
247 an initial concentration of 10 mg/L. Nanoplastics at 100–500 $\mu\text{g/L}$ can exert
248 widespread toxicity to marine organisms including bivalves, sea urchins, algae, and
249 bacteria (Gonçalves & Bebianno, 2021). Adopting the 1% seawater salinity threshold
250 as a reference for nanoplastic concentrations facilitates comparisons of migration
251 patterns between nanoplastics and dissolved salts under freshwater extraction
252 scenarios in idealized strip-shaped islands, while incorporating the biological toxicity
253 of nanoplastics as a critical constraint.

254 Concurrently, the distribution of nanoplastics within freshwater lenses is
255 characterized by comparing the volume reduction rate (VR) of freshwater lenses over
256 a given time period:

$$VR = \frac{V_0 - V_w}{V_0} \quad (9)$$

257 where V_w represents the volume of freshwater lenses surrounded by nanoplastics
258 pollution [L^3], V_0 represents the volume of freshwater lenses surrounded by saline
259 water [L^3].

260 Accounting for the implications of the transition zone theory for groundwater
 261 pumping practices, the following indicator is defined: the ratio of the actual maximum
 262 safe extraction capacity to the theoretical maximum safe extraction capacity (*ASYR*):

$$ASYR = \frac{Q_{Amax}}{Q_{Tmax}} \quad (10)$$

263 where Q_{Amax} represents the actual maximum safe extraction volume [L^3T^{-1}], Q_{Tmax}
 264 represents the theoretical maximum safe extraction volume [L^3T^{-1}]

265 Taking into account the potential reduction in groundwater extraction capacity
 266 induced by nanoplastic contamination, the following indicator is defined: the ratio of
 267 the maximum safe extraction capacity reduction caused by nanoplastic retention to the
 268 maximum safe extraction capacity (*RRSY*):

269

$$RRSY = \frac{Q_{Amax} - Q_{Smax}}{Q_{Amax}} \quad (11)$$

270 where Q_{Smax} represents the maximum safe extraction volume without nanoplastic
 271 influence [L^3T^{-1}].

272 Table 2 provides a systematic description of the representative roles of the three
 273 evaluation metrics used in this paper:

274 **Table 2.** Summary of Evaluation Indicators and Their Functions

Symbol	Full name	Description
VR	Volume reduction rate	Quantifies the shrinkage degree of usable freshwater lens volume under nanoplastic contamination.
ASYR	Ratio of the actual maximum safe extraction capacity to the theoretical	Evaluates the reduction degree of practical safe extraction capacity relative to the theoretical threshold.

	maximum safe extraction	
	capacity	
	Ratio of the maximum safe	
	extraction capacity	Assesses the additional loss of safe
RRSY	reduction caused by	extraction capacity specifically caused by
	nanoplastic retention to the	nanoplastic retention and contamination.
	maximum safe extraction	
	capacity	

275

276 **2.4 Model Calibration**

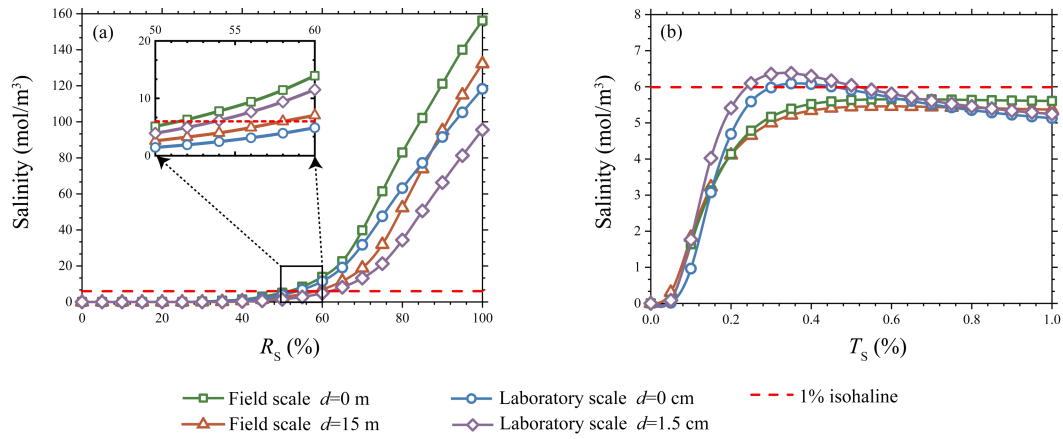
277 This study examined the migration patterns of two synthetic nanoplastics
278 (PS-Pd-1 and PS-Pd-2) that exhibit contrasting hydrophobicity. The detailed synthesis
279 protocols are available in Supplementary Materials (Text S2). To ensure model
280 accuracy, migration parameters for nanoplastics in quartz sand (Table 1) were
281 validated using column experiment data from Liu et al. (2025). The experimental
282 setup and methodology are detailed in Text S3 and Fig. S1, with calibration processes
283 and results illustrated in Fig. S2 and S3. The primary objective was to quantify how
284 differential nanoplastic-solid phase interactions influence contamination levels in
285 freshwater lenses (Amirmoshiri et al., 2020; Wang et al., 2021). As summarized in
286 Table 1, PS-Pd-1 exhibits strong solid-phase adsorption capacity, whereas PS-Pd-2
287 demonstrates weaker adsorption. Given potential scale-dependence in nanoplastic
288 transport parameters, current research remains largely focused on laboratory-scale
289 investigations (Johnson, 2020; Li et al., 2021; Liu et al., 2025).

290 A single-well extraction scheme was implemented in the central region of an
291 idealized strip island aquifer. The maximum safe extraction rate, calculated based on
292 sharp-interface theory, served as the baseline scenario. However, the applicability of
293 this theoretical maximum for island freshwater lenses requires critical re-evaluation,
294 as previous sharp-interface analytical and numerical studies have largely neglected the
295 transition zone formed by salinity dispersion and diffusion—a factor addressed in

296 only limited corrections (Coulon et al., 2022). To determine a more accurate
297 maximum safe extraction rate, a series of numerical simulations with predefined
298 pumping rates were conducted to calibrate both laboratory-scale and field-scale
299 conceptual models.

300 Although Tang et al. (2021) provided preliminary numerical validation via Fig.
301 S4(a)(b), their simulations omitted the effects of the unsaturated zone and the salinity
302 transition zone. In contrast, our validation-based simulations (Fig. S4(c)(d)), which
303 incorporate the unsaturated zone and employ dispersion parameters consistent with
304 Chen et al. (2024b), indicate that the 1% salinity contour exceeds the well bottom
305 elevation by 2.03 m. This signifies that pumping-induced salinity surpasses regulatory
306 thresholds, necessitating a reduction in extraction volume.

307 The relationship between well salinity and the extraction volume ratio (actual to
308 theoretical) in numerical simulations is illustrated in Fig. 3. Results confirm that the
309 presence of the unsaturated and transition zones reduces the extraction capacity to
310 50% – 60% of the theoretical maximum (Q_{Tmax}). Specifically, under laboratory
311 conditions, the maximum safe extraction capacity decreased to 61% and 53% of Q_{Tmax}
312 for shallow ($d=0$ cm) and deep ($d=1.5$ cm) extraction scenarios, respectively (Fig.
313 3(a)). Corresponding field-scale simulations showed reductions to 57% and 51% of
314 Q_{Tmax} for shallow ($d=0$ m) and deep ($d=15$ m) extraction. The temporal evolution of
315 well salinity during freshwater lens re-stabilization (Fig. 3(b)) further demonstrates
316 that salinity stabilization occurs within 12 minutes at the laboratory scale but requires
317 approximately 4.5 years at the field scale, highlighting significant temporal disparities
318 influenced by scale effects.



319

320 Fig. 3. Variations in well salinity as a function of the ratio of extraction volume to
 321 theoretical maximum (R_s) and the ratio of time to theoretical equilibrium time (T_s)
 322 during pumping at different depths in numerical simulations, measured at both field
 323 and laboratory scales: (a) Well salinity versus extraction volume, with the magnified
 324 region indicating the extraction volume range where well concentration approaches
 325 the 1% isohaline; (b) Temporal concentration variations for wells with salinity near
 326 the 1% isohaline in panel (a).

327 3. Results and Discussion

328 3.1 Distribution Patterns of Nanoplastics Under Pumping Conditions

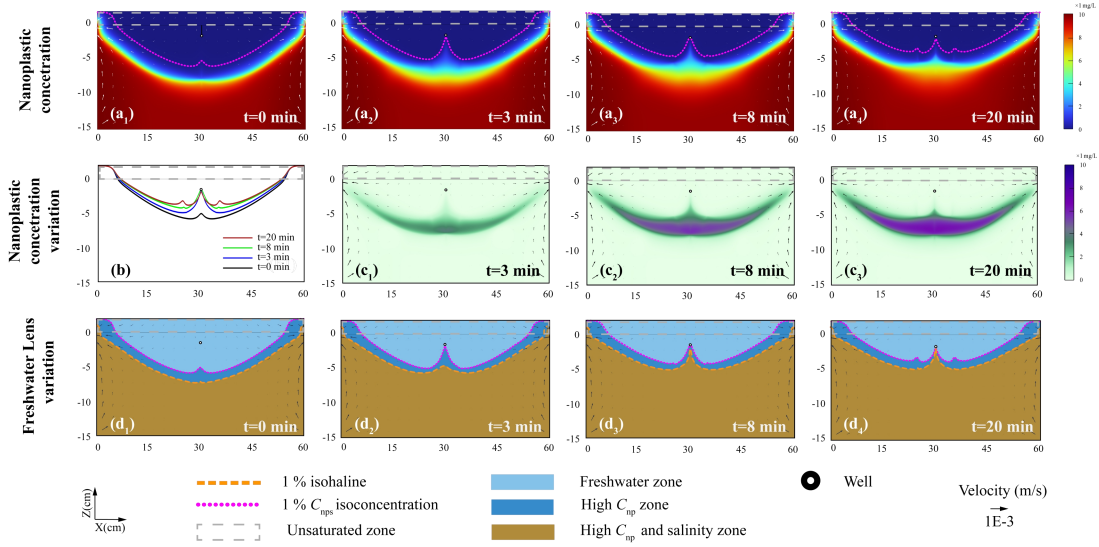
329 Hydrophobic nanoplastics (NPs) were selected as the primary research focus of
 330 this study. Text S4 and Fig. S5 demonstrate that hydrophobic nanoplastic particles
 331 exhibit higher mobility and pose more significant hazards than hydrophilic
 332 counterparts under simulated single-well pumping conditions.

333 Fig. 4(a₁-a₄) illustrates an “upper cone” phenomenon in nanoplastic
 334 concentrations during pumping, analogous to that of salinity. Fig. 4(a₁) reveals that
 335 highly dispersive nanoplastics may form anomalous distributions in the central
 336 banded region of the island—a zone previously referred to as the “stagnation zone”
 337 (Wang et al., 2023). Nearshore aquifers on both sides of the island undergo intense
 338 convection, driven by groundwater discharge to the sea and seawater intrusion
 339 induced by density currents. At the laboratory scale, this convective zone spans

340 approximately 10 cm; at the field scale, it extends to around 100 meters, where
341 groundwater Darcy velocities exceed 1×10^{-3} m/s. In contrast, velocities within the
342 central “stagnation zone” remain below 1×10^{-8} m/s. This zone is dominated by weak
343 convection, with material transport in groundwater primarily governed by dispersion
344 and interactions with the solid phase.

345 Fig. 4(b) presents dynamic nanoplastic isoconcentration lines at the wellhead,
346 where concentrations first increase and then decrease—indicating that wellhead
347 nanoplastics are influenced by the “stagnation zone”. The discrepancy in migration
348 behavior between nanoplastics and dissolved solutes stems primarily from their
349 distinct physicochemical properties: as colloidal particles, nanoplastic migration is
350 regulated not only by advection-dispersion but also by particle-medium interactions
351 (e.g., adsorption-desorption, clogging, and filtration). Fig. 4(c₁-c₃) depicts variations
352 in nanoplastic concentrations. Considering the nanoplastic concentration threshold
353 resulted in an additional 37.48% reduction in the usable freshwater lens area, while
354 the maximum depth of freshwater zones affected by nanoplastic contamination
355 increased by 0.030 m.

356 Fig. 4(d₁-d₄) compares the distribution patterns of salinity and nanoplastics,
357 revealing that nanoplastics exceeding 1% of the critical nanoplastic concentration
358 (C_{nps}) are concentrated within freshwater lens layers. With the disappearance of the
359 original “stagnation zone”, a new flow field transition zone is formed, triggering the
360 emergence of a new “stagnation zone”. The proportion of the freshwater lens
361 occupied by the nanoplastic transition zone (dark blue areas in Fig. 4(d₁-d₄)) increased
362 from 30.27% to 41.24%. Compared to dissolved solutes, nanoplastics possess larger
363 hydrodynamic diameters and unique surface properties, leading to distinctive
364 migration patterns in porous media.



365

366 Fig. 4. Distribution and concentration dynamics of PS-Pd-2 hydrophobic nanoplastics
 367 and corresponding freshwater lens alterations at the laboratory scale (60 cm×17 cm)
 368 during pumping ($R_S = 53\%$) in numerical simulations: (a₁-a₄) freshwater lenses
 369 demarcated by the 1% isoconcentration line of PS-Pd-2 hydrophobic nanoplastics at 0,
 370 3, 8 and 20 minutes post-pumping, (b) temporal variation of the 1% C_{nps}
 371 isoconcentration line, (c₁-c₃) net concentration variations relative to the baseline (0
 372 min) at 3, 8 and 20 minutes post-pumping, (d₁-d₄) spatial offset between the 1%
 373 isohaline and 1% C_{nps} isoconcentration line around the freshwater lens.

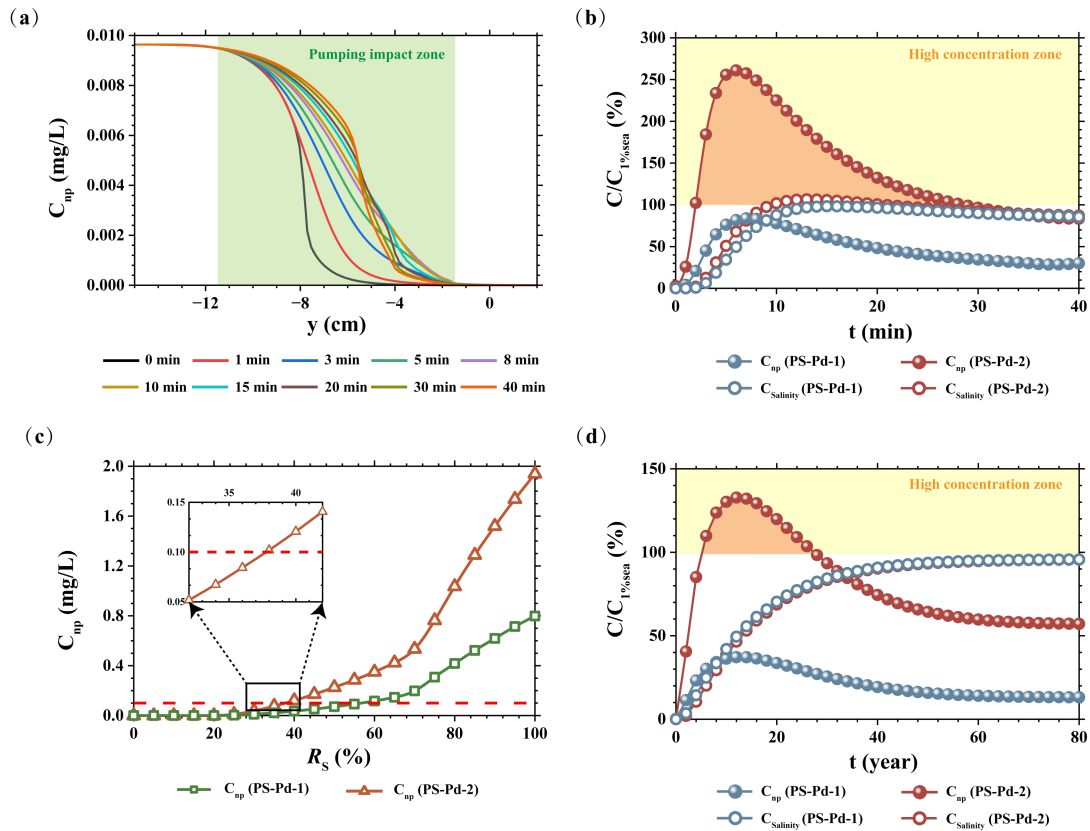
374 Fig. 5(a) presents the vertical concentration profile of nanoplastics at the
 375 wellhead, further validating the aforementioned mechanism. Prior to pumping
 376 initiation, the nanoplastic transition zone was situated 0.07 - 0.10 m below the well
 377 bottom. Following pumping initiation, the transition zone underwent a rapid upward
 378 migration and expansion to 0.02 m below the well bottom. Thirty minutes
 379 post-pumping, although the transition zone exhibited a slight recession, a stable
 380 transition zone was maintained at 0.06 m below the well bottom, while a new steep
 381 transition zone formed at 0.03 m. Nanoplastic concentrations at the wellhead
 382 increased markedly within the first 4 minutes, started to decline after 8 minutes,
 383 stabilized at 30 minutes post-pumping, and ultimately converged with the
 384 concentration trends of chloride (Cl⁻), indicating that solute and colloidal transport are

385 governed primarily by convection. The observed transport behavior can be interpreted
386 through the lens of effective dispersion parameters. In porous media transport
387 modeling, the macroscopic dispersion coefficient in advection-dispersion equations
388 serves as an effective parameter that implicitly captures the integrated effects of
389 various pore-scale processes, including particle-pore interactions, flow path tortuosity,
390 and temporary retention at pore throats. While these microscopic processes are not
391 explicitly resolved in the current continuum-scale model, their integrated effects are
392 reflected in the calibrated dispersion parameters.

393 Fig. 5(b) illustrates the temporal concentration variations of hydrophilic and
394 hydrophobic nanoplastics, both of which exhibit an initial increase followed by a
395 subsequent decrease. During the initial pumping phase (0 - 6 min), high-concentration
396 nanoplastics in the immediate vicinity of the well were the primary fraction extracted
397 by pumping, leading to a sharp concentration increase to a peak of 2.489% C_{nps} . With
398 prolonged pumping (6 - 32 min), peripheral groundwater with relatively low
399 nanoplastic concentrations gradually entered the pumping-affected zone. The original
400 stagnation zone was reconfigured under the influence of pumping, with new
401 stagnation zones emerging on both sides of the well. The system eventually attained a
402 state of dynamic equilibrium after 32 min of pumping, with nanoplastic
403 concentrations stabilizing at a steady level. Notably, salinity variations under distinct
404 contamination scenarios involving hydrophilic and hydrophobic nanoplastics also
405 influenced this process. This phenomenon is hypothesized to originate from an
406 approximate 40% reduction in hydraulic conductivity, which is induced by the
407 solid-phase enrichment of hydrophilic nanoplastics in specific central regions of the
408 study domain.

409 With respect to the distinct distribution characteristics of wellborne hydrophobic
410 nanoplastics presented in Fig. 5(b), which diverge from those of salinity, the
411 application of a 1% concentration threshold to nanoplastics (consistent with the
412 salinity threshold) results in wellhead nanoplastic concentrations exceeding this
413 criterion for more than 80% of the duration prior to the attainment of a stable system

414 state. To mitigate the adverse impacts of the extensive dispersion of hydrophobic
415 nanoplastics on the quality of pumped groundwater, Fig. 5(c) shows the relationships
416 between wellhead nanoplastic concentrations and cumulative pumped water volume
417 for hydrophilic and hydrophobic nanoplastics. Under the theoretical maximum safe
418 pumping rate, hydrophobic nanoplastics accumulate at the wellhead to a concentration
419 of 1.939 mg/L during the initial pumping phase. To reduce the initial wellhead
420 nanoplastic concentrations to below the 1% C_{nps} threshold, the actual maximum safe
421 pumping rate must be further reduced to 37% of the theoretical maximum safe
422 pumping rate. Fig. 5(d) indicates that a similar phenomenon is observable in wellhead
423 nanoplastic concentrations at the field scale, where nanoplastics at such
424 concentrations are still rapidly entrained into the pumping well—indicating that the
425 enrichment mechanism driven by high nanoplastic dispersibility remains valid at the
426 field scale. High-concentration nanoplastic influxes at the wellhead persisted from
427 years 5 to 28 at the field scale. Conversely, nanoplastic concentrations in the upper
428 cone region are comparatively lower, with those in the island ' s pumping wells
429 reaching only 1.329% C_{nps} . A detailed elucidation of the underlying mechanisms for
430 this phenomenon is presented in Section 3.2.



431

432 Fig. 5. Concentration dynamics at laboratory and field scales and their responses to

433 pumping rate adjustments in numerical simulations: (a) 1% C_{nps} isoconcentration line

434 variation along the central axis ($x=30$ cm) at laboratory scale; (b) Temporal variations

435 in salinity and nanoplastic concentrations for hydrophilic and hydrophobic

436 nanoplastics at laboratory scale; (c) Well nanoplastic concentration as a function of

437 pumped volume-to-theoretical maximum ratio (R_s) for groundwater nanoplastics of

438 distinct hydrophilic-hydrophobic properties; (d) Temporal variations in well salinity

439 and nanoplastic concentrations for hydrophilic and hydrophobic nanoplastics at field

440 scale.

441 3.2 Scale Effects on Nanoplastic Transport

442 In field-scale simulations, the background concentration of hydrophobic

443 nanoplastics was set to $1 \mu\text{g/L}$ (C_{nps}). Dispersion parameters were adjusted based on

444 scaling-up experience (Gelhar et al., 1992), with the corresponding simulation results

445 presented in Fig. 6. Fig. 6(a₁) shows that following stabilization of the freshwater lens,

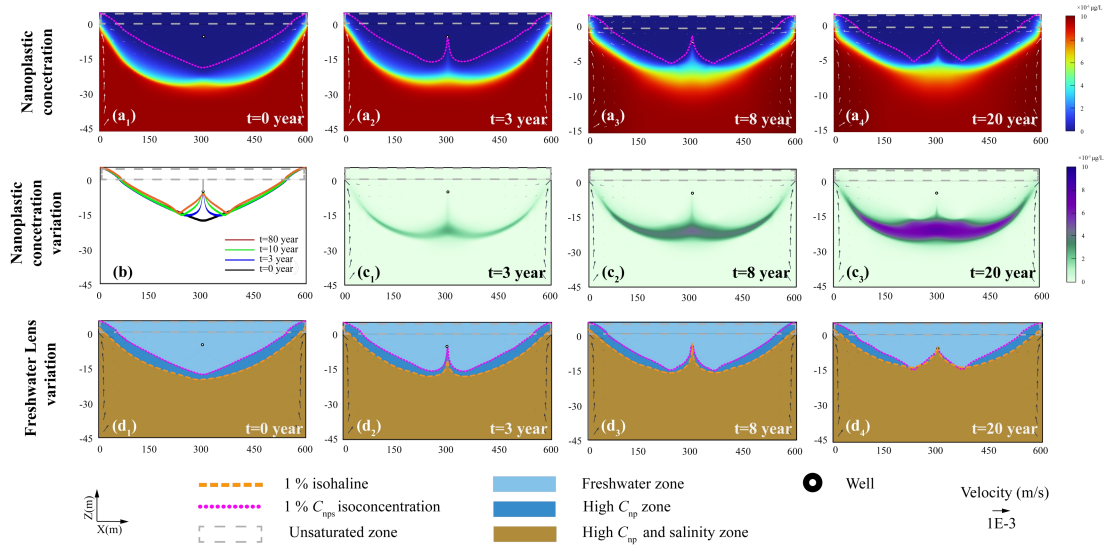
446 the 90%–10% C_{nps} transition zone in the central island region thickened to more than

447 10 m, yet no prominent dispersion-driven upward cone formed in the island's core

448 area. Scale effects exert their influence primarily in two aspects: with increasing scale,
449 the heterogeneity of the aquifer medium becomes more complex, which may mask the
450 unique migration behavior of nanoplastics. Additionally, streamline curvature is
451 reduced and flow velocity distributions are more homogeneous at larger scales,
452 thereby reducing the influence of local streamline curvature on particle migration.

453 Upon pumping initiation at the field scale, the depth of the freshwater lens
454 decreased from 20.168 m to 13.785 m, while the maximum depth of the freshwater
455 lens encircled by nanoplastics decreased from 17.943 m to 14.610 m. Fig. 6(c₁-c₃)
456 depicts variations in nanoplastic concentration within the lens: the volumetric fraction
457 of nanoplastics occupying the freshwater lens decreased from 31.48% to 23.40%, a
458 trend that deviates from the increasing pattern observed at the laboratory scale. Fig.
459 6(d₁-d₄) reveals the existence of a ~3 m-thick residual nanoplastic-bearing layer
460 within the freshwater lens, with concentrations at 1-5% of the nanoplastic
461 concentration in seawater. Upon stabilization of pumping, the transition zone migrated
462 upward toward the lateral high-velocity discharge zones but no new upward cone was
463 generated. At the field scale, the enhancement of nanoplastic dispersion relative to
464 solute dispersion was no longer pronounced, a phenomenon likely due to improved
465 flow stability and inherent scale effects. In addition, the residence time of colloidal
466 filtration and entrainment processes is extended at this scale, which may consequently
467 modify the final spatial distribution of nanoplastics.

468



469

470 Fig. 6. Hydrophobic nanoplastic concentration dynamics and corresponding
 471 freshwater lens alterations at field scale (600 m×50 m) during pumping ($R_s = 51\%$) in
 472 numerical simulations: (a₁-a₄) Freshwater lenses demarcated by the 1% PS-Pd-2
 473 nanoplastic isoconcentration line at 0, 3, 8 and 20 years post-pumping; (b) 1% C_{nps}
 474 isoconcentration line variation; (c₁-c₃) Net nanoplastic concentration variations
 475 relative to the initial time point (0 year) at 3, 8 and 20 years post-pumping; (d₁-d₄)
 476 Spatial offset between the 1% isohaline and 1% C_{nps} isoconcentration line around the
 477 freshwater lens.

478 3.3 Sensitivity Analysis

479 Four factors were selected for analysis, with the VR , $ASYR$, and $RRSY$ metrics
 480 employed to evaluate nanoplastic contamination in freshwater and freshwater lenses,
 481 as well as its implications for pumping operations.

482 Fig. 7(a₁, b₁) demonstrates that nanoplastic dispersivity exhibits a significant
 483 correlation with VR , and nanoplastic dispersivity exerts a notable influence on
 484 pumping efficiency. When nanoplastic dispersivity is lower than that of solutes, the
 485 distribution range of nanoplastics closely approximates that of solutes, resulting in a
 486 narrow transition zone, while Q_{Amax} is exclusively governed by salinity. When
 487 nanoplastic dispersivity equals that of solutes, the nanoplastic-constrained freshwater
 488 lens zone nearly overlaps with the salinity-defined freshwater lens zone. As

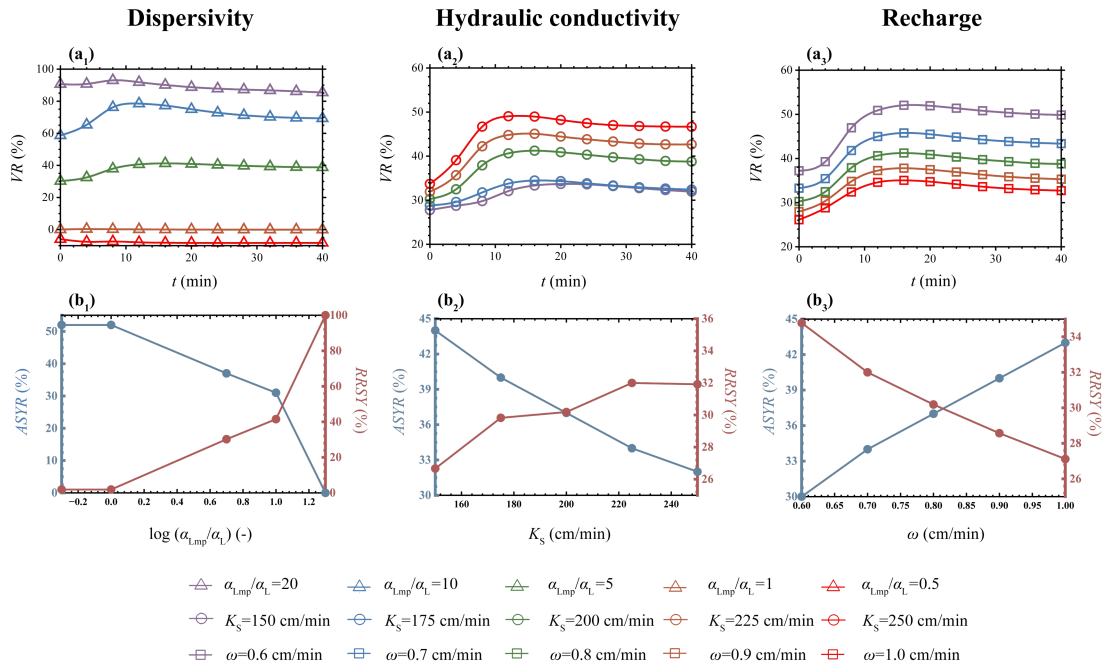
489 dispersivity increases to 10 times that of solutes, the volume of freshwater lenses
490 decreases by approximately 30%. When the effective dispersivity of nanoplastics
491 exceeds 17 times that of dissolved salts, the expanded dispersion range causes the 1%
492 C_{nps} isoconcentration line to cover the wellhead area. The high sensitivity of
493 nanoplastic behavior to dispersivity stems from their particulate nature: nanoplastics
494 migrate not only via hydraulic dispersion but also through mechanisms such as
495 Brownian motion, gravitational settling, and media interception. High dispersivity
496 reflects the selective migration capacity of nanoplastics within complex pore
497 structures, which is closely associated with their surface properties and hydrodynamic
498 characteristics.

499 Fig. 7(a₂,b₂) reveals that VR gradually increases with rising hydraulic
500 conductivity. At a hydraulic conductivity of 250 cm/min, 46.68% of the freshwater
501 lens area is occupied by high-concentration nanoplastics. Under pumping conditions,
502 both high hydraulic conductivity and high-permeability media result in a significant
503 reduction in the usable portion of freshwater lens layers surrounded by nanoplastics.
504 Aquifer hydraulic conductivity is another critical parameter regulating solute
505 migration and retention. Previous studies have demonstrated that higher hydraulic
506 conductivities result in reduced freshwater lens volumes and correspondingly
507 decreased groundwater availability (Bailey and Jenson, 2014; Cui et al., 2021; Gao et
508 al., 2025). The spatial distribution and magnitude of freshwater lenses surrounded by
509 nanoplastics are consistent with these findings. High hydraulic conductivity
510 accelerates freshwater discharge on both sides of the island, reducing the area where
511 freshwater lenses can maintain equilibrium. For nanoplastics, increased hydraulic
512 conductivity enhances flow velocity and convective transport capacity, thereby
513 facilitating their intrusion into freshwater lenses.

514 Recharge rates were used to represent effective rainfall infiltration on the island.
515 Fig. 7(a₃) shows that recharge significantly reduces the spatial distribution density of
516 nanoplastics within freshwater lenses, with this effect being pronounced both before
517 and after pumping. Increased recharge leads to a decrease in VR ; when recharge rises

518 to 1.0 cm/min, VR declines to 33%. Conversely, when recharge drops below 0.65
519 cm/min, the final variation in VR also weakens, suggesting that nanoplastic
520 concentrations are more difficult to mitigate with increased pumping intensity. Fig.
521 7(b₃) illustrates that enhanced recharge reduces the volume occupied by
522 high-concentration nanoplastics in freshwater lenses, significantly increasing
523 exploitable freshwater volume and alleviating the impact of nanoplastics on maximum
524 safe pumping rates. Previous studies indicate that the volume and thickness of island
525 freshwater lenses are positively correlated with precipitation (Zheng et al., 2025). The
526 "flushing effect" of recharge on nanoplastic distribution likely operates through two
527 mechanisms: first, recharge acts as the main source of freshwater storage in lenses. As
528 the freshwater lens area expands, the thick transition zone formed by hydrophobic
529 nanoplastics remains unaffected by convection and maintains a constant thickness,
530 leading to a reduced proportion of nanoplastics despite unchanged total volume.
531 Second, increased recharge may expand the strong convection zones on both sides of
532 the seawater boundary, shrinking the central "stagnation zone" and thereby relatively
533 weakening dispersion effects.

534 Among the analyzed media and environmental conditions, dispersivity emerges
535 as the key parameter governing nanoplastic retention behavior in freshwater lenses,
536 with high dispersivity exerting the most pronounced inhibitory effect on Q_{Amax} .



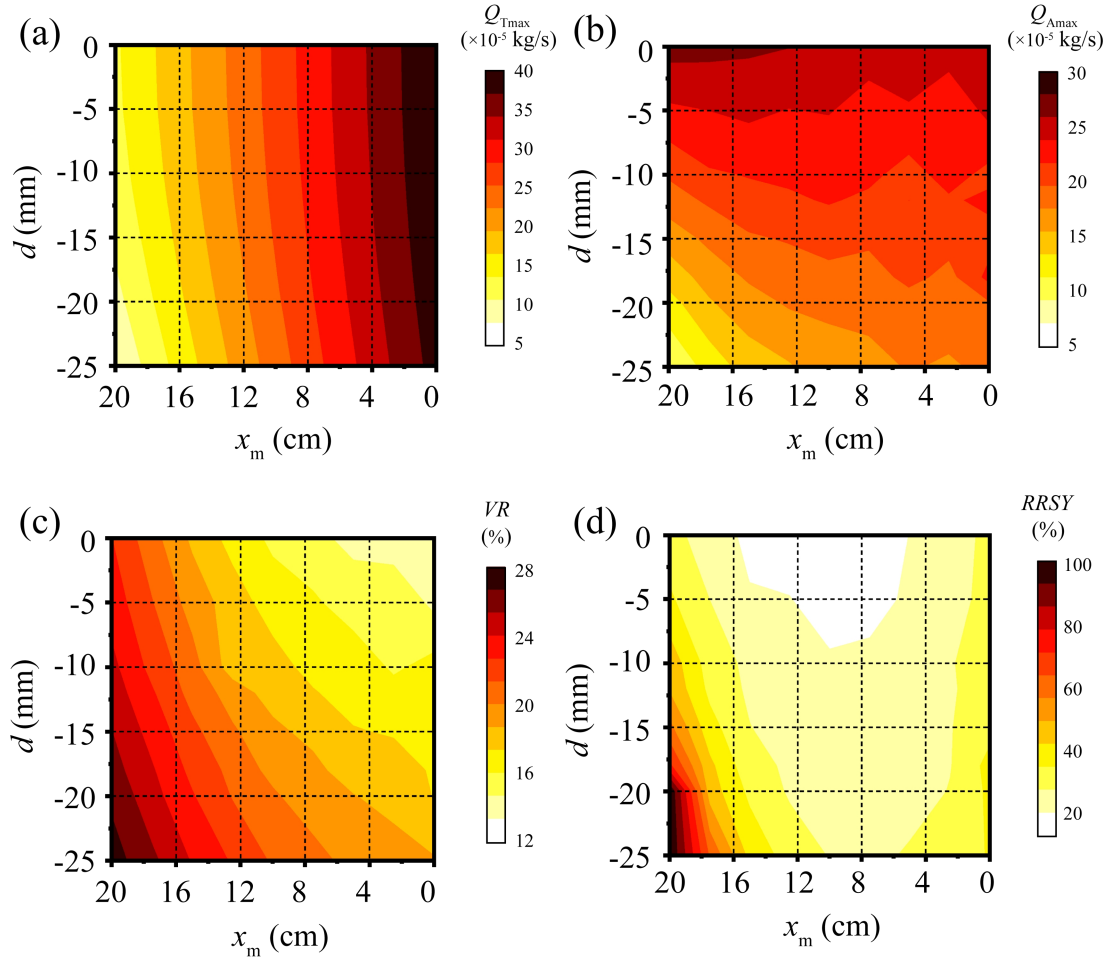
537

538 Fig. 7. The volume reduction rate of freshwater lenses (VR), the ratio of actual
 539 maximum safe extraction capacity to theoretical maximum safe extraction capacity
 540 ($ASYR$), and the ratio of maximum safe extraction capacity reduction due to
 541 nanoplastic retention to maximum safe extraction capacity ($RRSY$) versus (a₁-a₃)
 542 dispersivity, (b₁-b₃) hydraulic conductivity, and (c₁-c₃) recharge rate in numerical
 543 simulations.

544 Fig. 8(a) and (b) present the theoretically derived maximum safe pumping rate
 545 near the freshwater lens center (Tang et al., 2021) and the actual maximum safe
 546 pumping rate, respectively. Under standard pumping conditions, the presence of a
 547 transition zone reduces the effective area of the freshwater lens by 16.12% and its
 548 thickness by 7.77 m. The position of pumping wells directly influences pumping rates:
 549 as the distance from the central region increases, pumping rates decrease linearly, as
 550 expressed in Equation (5). Simulation results demonstrate that the maximum safe
 551 pumping rate of freshwater lenses does not exhibit a perfect linear correlation with the
 552 distance from the surface central axis. During shallow pumping, higher rates may
 553 even be achieved near the coastal sides due to the low-velocity zone in the center.
 554 Under salinity-based constraints, the actual maximum safe pumped volume occurs at
 555 the pumping point ($x_m=20$ cm, $y=0$ cm), corresponding to approximately two-thirds of

556 the half-width of the island from the central axis, with a pumping rate of 2.667×10^{-5}
557 kg/s (200% of the theoretical value). At the center, the rate decreases to 2.480×10^{-5}
558 kg/s, equivalent to 62% of the theoretical value. Under idealized strip-shaped island
559 hydrodynamic conditions, seawater infiltrates from both bottom sides, forming an
560 outflow zone at the top of the coastline, with a "stagnation zone" emerging in the
561 island center—a phenomenon confirmed in previous studies. Owing to the slow,
562 predominantly vertical flow in the central region, residual brackish water persists and
563 disperses upward primarily via vertical dispersion. Thus, for single-well pumping
564 projects on small idealized strip-shaped islands, central pumping may not be optimal,
565 whereas lateral single-well operations can yield higher freshwater outputs. For deep
566 pumping, given that freshwater lenses on such islands are approximately semicircular,
567 deeper pumping is feasible near the center.

568 Fig. 8(c) illustrates that nanoplastic concentration constraints reduce freshwater
569 lens volume by 13-28%, with more significant reductions in areas farther from the
570 island's surface central axis, attributed to the uneven distribution of the nanoplastic
571 transition zone. With respect to the reduction in maximum safe pumping rates, Fig.
572 8(d) demonstrates the decline in pumped volumes at the island center when
573 nanoplastic concentration limits are considered. Centered at the pumping point
574 ($x_m=10$ cm, $y=0$ cm), the maximum safe pumped volume gradually decreases with
575 increasing distance from this center due to nanoplastic concentration restrictions. Near
576 the seawater boundary, the transition zone completely covers the area within 10 cm of
577 the shoreline. Under the 1% C_{nps} concentration limit, regions deeper than 25 mm are
578 designated as non-exploitable zones. This phenomenon arises because the nanoplastic
579 transition zone is relatively extended in the island's central region. Certain central
580 regions exhibit pathway advantages, facilitating faster nanoplastic accumulation into
581 wells. Near the seawater boundary, exploitable volumes decrease due to the influence
582 of seawater nanoplastic source concentrations. Consequently, the combined effect of
583 these two factors results in the highest exploitable volumes occurring in the upper
584 regions near the central axis.



585

586 Fig. 8. Effects of pumping depth (d) and horizontal distance from the island center (x_m)
 587 on (a) theoretical maximum safe extraction rate (Q_{Tmax}), (b) actual maximum safe
 588 extraction rate (Q_{Amax}), (c) freshwater lens volume reduction rate (VR), and (d)
 589 reduction ratio of safe yield caused by nanoplastic retention ($RRSY$) in the idealized
 590 strip-island aquifer.

591

592 4. Conclusion

593 This study established a coupled variable-density groundwater flow and transport
 594 model to explore nanoplastic migration in the freshwater lenses of idealized strip
 595 islands under pumping scenarios. By integrating laboratory-calibrated parameters
 596 with field-scale simulations, we identified fundamental differences between

597 nanoplastic and traditional solute transport processes and evaluated their implications
598 for groundwater management in island aquifers. Key conclusions are summarized as
599 follows:

600 (1) Nanoplastic transport differs fundamentally from dissolved salt transport
601 within the freshwater lenses of idealized strip-island aquifers during groundwater
602 pumping. In contrast to dissolved salts, whose behavior is mainly regulated by
603 advection and dispersion, nanoplastics are further affected by particle-specific
604 processes, such as adsorption-desorption, clogging, and filtration. The higher effective
605 dispersivity leads to earlier breakthrough at extraction wells and the development of
606 broader contaminant transition zones compared to salinity alone under
607 pumping-induced upconing conditions in coastal island aquifers.

608 (2) Transport behavior exhibits strong scale dependence in strip-island
609 freshwater lens systems under pumping stress. Laboratory-scale simulations showed
610 rapid contamination and prominent "upper cone" formation within minutes, whereas
611 field-scale simulations demonstrated attenuated upward coning and much longer
612 stabilization times on the order of years. This contrast highlights the importance of
613 multi-scale modeling when extrapolating experimental results to real-world island
614 aquifers subject to freshwater extraction and seawater intrusion.

615 (3) Dispersivity is the dominant control on nanoplastic risk for pumping wells
616 tapping freshwater lenses in strip-island coastal aquifers. Among the evaluated
617 parameters, nanoplastic dispersivity exerts the strongest influence on contaminant
618 accumulation in extraction wells, with hydraulic conductivity and recharge rates
619 playing secondary but important roles. When nanoplastic dispersivity exceeds
620 approximately 17 times that of dissolved solutes, the contaminant plume can fully
621 envelop the well screen, reducing the maximum safe extraction rate to 37-50% of the
622 salinity-based thresholds under island pumping scenarios.

623 (4) Well placement strategies must account for nanoplastic transition zones.
624 Traditional guidelines based solely on salinity intrusion may not minimize

625 contamination risks. Simulations suggest that central pumping locations are not
626 always optimal; lateral well placement can increase freshwater yield, although the
627 optimal position depends on whether salinity or nanoplastic concentration is used as
628 the limiting criterion.

629 Several simplifying assumptions were adopted in this study, including
630 homogeneous aquifer properties, idealized boundary conditions, and limited
631 representation of nanoplastic diversity. In practice, aquifer heterogeneity, tidal
632 fluctuations and storm events may further influence the groundwater flow field and,
633 consequently, the transport of substances. Furthermore, the diverse properties of
634 environmental nanoplastics such as particle size distribution, aging state and surface
635 chemistry will also bring additional impacts on their migration. In addition, only two
636 types of synthetic nanoplastics were considered in this study, whereas natural systems
637 contain a broader and more complex spectrum of particles. Despite these limitations,
638 the present study establishes a mechanistic framework for evaluating nanoplastic
639 transport in coastal freshwater lenses. By coupling variable-density flow with
640 particle-specific transport processes and quantifying impacts on safe extraction
641 thresholds, this study provides clear practical implications for well design, pumping
642 optimization, and groundwater management on small islands. Future research should
643 perform heterogeneous aquifer simulations, consider dynamic tidal and sea-level rise
644 scenarios, and adopt more realistic natural micro/nanoplastic properties to further
645 improve prediction accuracy and practical applicability for water security in
646 plastic-polluted coastal environments.

647 **Data availability**

648 The data of this study can be found in Zheng (2026,
649 <https://zenodo.org/records/19150343>).

650 **Author contributions**

651 TYZ: Conceptualization, Writing-Original Draft, Methodology, Resources,
652 Writing-Review and Editing, Funding acquisition, Supervision.

653 CXM: Investigation, Software, Writing-Original Draft, Writing-Review and Editing,
654 Visualization, Data Curation, Conceptualization.

655 SBG: Methodology, Formal Analysis, Investigation, Visualization, Writing-Review
656 and Editing.

657 JL: Writing-Review and Editing, Methodology, Supervision, Conceptualization.

658 **Competing interests**

659 The contact author has declared that none of the authors has any competing interests.

660 **Financial support**

661 This work was supported by the National Natural Science Foundation of China (No.
662 42422207), Taishan Scholars Program of Shandong Province (No. tsqn202408078)
663 and the Postdoctoral Fellowship Program of CPSF under Grant Number
664 GZC20250290.

665

666 References

- 667 Abdoulhalik, A., & Ahmed, A. A. (2018), Transient investigation of saltwater upconing in
668 laboratory-scale coastal aquifer, *Estuarine, Coastal and Shelf Science*, 214, 149-160.
669 <https://doi.org/10.1016/j.ecss.2018.09.024>.
- 670 Al Harraq, A., & Bharti, B. (2022), Microplastics through the Lens of Colloid Science, *ACS*
671 *Environmental Au*, 2(1), 3-10. <https://doi.org/10.1021/acsenvironau.1c00016>.
- 672 Alkindi, A., Al-Wahaibi, Y., Bijeljic, B. & Muggeridge, A. (2011), Investigation of longitudinal
673 and transverse dispersion in stable displacements with a high viscosity and density contrast
674 between the fluids. *Journal of Contaminant Hydrology*, 120-121, 170-183.
675 <https://doi.org/10.1016/j.jconhyd.2010.06.006>.
- 676 Alsumaiei, A. A., & Bailey, R. T. (2018), Quantifying threats to groundwater resources in the
677 Republic of Maldives Part I: Future rainfall patterns and sea-level rise, *Hydrological*
678 *Processes*, 32(9), 1137-1153. <https://doi.org/10.1002/hyp.11480>.
- 679 Amirmoshiri, M., Zhang, L., Puerto, M. C., Tewari, R. D., Bahrim, R. Z. B. K., Farajzadeh, R.,
680 Hirasaki, G. J., & Biswal, S. L. (2020), Role of Wettability on the Adsorption of an Anionic
681 Surfactant on Sandstone Cores, *Langmuir*, 36(36), 10725-10738.
682 <https://doi.org/10.1021/acs.langmuir.0c01521>.
- 683 Babakhani, P., Bridge, J., Doong, R. A., & Phenrat, T. (2017), Continuum-based models and
684 concepts for the transport of nanoparticles in saturated porous media: A state-of-the-science
685 review, *Advances in colloid and interface science*, 246, 75-104.
686 <https://doi.org/10.1016/j.cis.2017.06.002>.
- 687 Babu, R., Park, N., & Nam, B. (2020), Regional and well-scale indicators for assessing the
688 sustainability of small island fresh groundwater lenses under future climate conditions,
689 *Environmental Earth Sciences*, 79(1), 47. <https://doi.org/10.1007/s12665-019-8773-3>.
- 690 Bailey, R. T., & Jenson, J. W. (2014), Effects of Marine Overwash for Atoll Aquifers:
691 Environmental and Human Factors, *Groundwater*, 52(5), 694-704.
692 <https://doi.org/10.1111/gwat.12117>.
- 693 Chen, G., Zou, Y., Xiong, G., Wang, Y., Zhao, W., Xu, X., Zhu, X., Wu, J., Song, F., & Yu, H.
694 (2024a), Microplastic transport and ecological risk in coastal intruded aquifers based on a
695 coupled seawater intrusion and microplastic risk assessment model, *Journal of hazardous*
696 *materials*, 480, 135996. <https://doi.org/10.1016/j.jhazmat.2024.135996>.
- 697 Chen, Q., Zhang, L., Shen, C., & Lu, C.(2024b), Effects of groundwater pumping on pore water
698 flow and salt transport in tide-controlled unconfined coastal aquifers, *Hydrological Processes*,
699 38(8), e15261. <https://doi.org/10.1002/hyp.15261>.
- 700 Coulon, C., Lemieux, J. M., Pryet, A., Bayer, P., Young, N. L., & Molson, J. (2022), Pumping
701 Optimization Under Uncertainty in an Island Freshwater Lens Using a Sharp-Interface
702 Seawater Intrusion Model, *Water Resources Research*, 58(8), e2021WR031793.
703 <https://doi.org/10.1029/2021WR031793>.
- 704 Cui, X., Zhu, C., Hu, M., Wang, R., & Liu, H. (2021), Permeability of porous media in coral reefs,
705 *Bulletin of Engineering Geology and the Environment*, 80(6), 5111-5126.
706 <https://doi.org/10.1007/s10064-020-02082-5>.
- 707 Dagan, G., & Bear, J. (1968), Solving The Problem Of Local Interface Upconing In A Coastal
708 Aquifer By The Method Of Small Perturbations, *Journal of Hydraulic Research*, 6(1), 15-44.

709 <https://doi.org/10.1080/00221686809500218>.

710 Dose, E. J., Stoeckl, L., Houben, G. J., Vacher, H. L., Vassolo, S., Dietrich, J., & Himmelsbach, T.
711 (2014), Experiments and Modeling of Freshwater Lenses in Layered Aquifers: Steady State
712 Interface Geometry, *Journal of Hydrology*, 509, 621-630.
713 <http://dx.doi.org/10.1016/j.jhydrol.2013.10.010>.

714 Gao, C., Zheng, T., Chang, Q., Zheng, X., Song, X., & Luo, J. (2025), Dynamics of Irregular
715 Freshwater Lenses Evolution in Thin Aquifers of Reclaimed Circular Islands, *Water*
716 *Resources Research*, 61(7), e2024WR038880. <https://doi.org/10.1029/2024WR038880>.

717 Gelhar, L. W., Welty, C., & Rehfeldt, K. R. (1992), A critical review of data on field-scale
718 dispersion in aquifers, *Water Resources Research*, 28(7), 1955-1974.
719 <https://doi.org/10.1029/92WR00607>.

720 Gonçalves, J. M., & Bebianno, M. J. (2021). Nanoplastics impact on marine biota: A review.
721 *Environmental Pollution*, 273, 116426. <https://doi.org/10.1016/j.envpol.2021.116426>.

722 Houben, G., & Post, V. E. A. (2017), The first field-based descriptions of pumping-induced
723 saltwater intrusion and upconing, *Hydrogeology Journal*, 25(1), 243-247.
724 <https://doi.org/10.1007/s10040-016-1476-x>.

725 Isobe, A., Iwasaki, S., Uchida, K., & Tokai, T. (2019), Abundance of non-conservative
726 microplastics in the upper ocean from 1957 to 2066, *Nature Communications*, 10(1), 417.
727 <https://doi.org/10.1038/s41467-019-08316-9>.

728 Johnson, W. P. (2020), Quantitative Linking of Nanoscale Interactions to Continuum-Scale
729 Nanoparticle and Microplastic Transport in Environmental Granular Media, *Environmental*
730 *Science & Technology*, 54(13), 8032-8042. <https://doi.org/10.1021/acs.est.0c01172>.

731 Ketabchi, H., Mahmoodzadeh, D., Ataie-Ashtiani, B., Werner, A. D., & Simmons, C. T. (2014),
732 Sea-level rise impact on fresh groundwater lenses in two-layer small islands, *Hydrological*
733 *Processes*, 28(24), 5938-5953. <https://doi.org/10.1002/hyp.10059>.

734 Koelmans, A. A., Redondo-Hasselerharm, P. E., Nor, N. H. M., de Ruijter, V. N., Mintenig, S. M. ,
735 & Kooi, M. (2022), Risk assessment of microplastic particles, *Nature Reviews Materials*,
736 7(2), 138-152. <https://doi.org/10.1038/s41578-021-00411-y>.

737 Koutnik, V. S., Leonard, J., Alkidim, S., DePrima, F. J., Ravi, S., Hoek, E. M. V., & Mohanty, S. K.
738 (2021), Distribution of microplastics in soil and freshwater environments: Global analysis
739 and framework for transport modeling, *Environmental pollution (Barking, Essex : 1987)*, 274,
740 116552. <https://doi.org/10.1016/j.envpol.2021.116552>.

741 Lee, J., Rolle, M. & Kitanidis, P. (2017), Longitudinal dispersion coefficients for numerical
742 modeling of groundwater solute transport in heterogeneous formations. *Journal of*
743 *Contaminant Hydrology*, 212, 41-54. <https://doi.org/10.1016/j.jconhyd.2017.09.004>.

744 Li, J., Liu, H., & Paul Chen, J. (2018), Microplastics in freshwater systems: A review on
745 occurrence, environmental effects, and methods for microplastics detection, *Water Research*,
746 137, 362-374. <https://doi.org/10.1016/j.watres.2017.12.056>.

747 Li, M., Zhang, M., Rong, H., Zhang, X., He, L., Han, P., & Tong, M. (2021), Transport and
748 deposition of plastic particles in porous media during seawater intrusion and
749 groundwater-seawater displacement processes, *Science of The Total Environment*, 781,
750 146752. <https://doi.org/10.1016/j.scitotenv.2021.146752>.

751 Liu, X., Zhao, R., Liu, M., Zheng, T., Hao, Y., Wang, C., Liu, L., Zhao, Y., Liu, Z., Dai, Y., Yue, T.,
752 Zhao, J., Wang, Z., & Xing, B. (2025). Transport of eco-corona coated nanoplastics in coastal

753 sediments. *Water research*, 284, 123893. <https://doi.org/10.1016/j.watres.2025.123893>.

754 Muskat, M. (1938), The flow of homogeneous fluids through porous media, *Soil Sci*, 46(2), 169.
755 https://journals.lww.com/soilsci/fulltext/1938/08000/the_flow_of_homogeneous_fluids_throu
756 [gh_porous.8.aspx](https://journals.lww.com/soilsci/fulltext/1938/08000/the_flow_of_homogeneous_fluids_throu).

757 Ranjan, V. P., Joseph, A., Sharma, H. B., & Goel, S. (2023), Preliminary investigation on effects of
758 size, polymer type, and surface behaviour on the vertical mobility of microplastics in a
759 porous media, *Science of The Total Environment*, 864, 161148.
760 <https://doi.org/10.1016/j.scitotenv.2022.161148>.

761 Ren, Z., Gui, X., Xu, X., Zhao, L., Qiu, H., & Cao, X. (2021), Microplastics in the
762 soil-groundwater environment: Aging, migration, and co-transport of contaminants - A
763 critical review, *Journal of hazardous materials*, 419, 126455.
764 <https://doi.org/10.1016/j.jhazmat.2021.126455>.

765 Ren, Z., Gui, X., Xu, X., Zhao, L., Qiu, H., Wang, X., & Cao, X. (2022), Weathering of
766 microplastics and their enhancement on the retention of cadmium in coastal soil saturated
767 with seawater, *Journal of hazardous materials*, 440, 129850.
768 <https://doi.org/10.1016/j.jhazmat.2022.129850>.

769 Sayre, R., Noble, S., Hamann, S., Smith, R., Wright, D., Breyer, S., Butler, K., Van Graafeiland,
770 K., Frye, C., Karagulle, D., Hopkins, D., Stephens, D., Kelly, K., Basher, Z., Burton, D.,
771 Cress, J., Atkins, K., Van Sistine, D. P., Friesen, B., Allee, R., Allen, T., Aniello, P., Asaad, I.,
772 Costello, M. J., Goodin, K., Harris, P., Kavanaugh, M., Lillis, H., Manca, E., Muller-Karger,
773 F., Nyberg, B., Parsons, R., Saarinen, J., Steiner, J., & Reed, A. (2019), A new 30 meter
774 resolution global shoreline vector and associated global islands database for the development
775 of standardized ecological coastal units, *Journal of Operational Oceanography*, 12(sup2),
776 S47-S56. <https://doi.org/10.1080/1755876X.2018.1529714>.

777 Sharan, A., Lal, A., & Datta, B. (2021), A review of groundwater sustainability crisis in the Pacific
778 Island countries: Challenges and solutions, *Journal of Hydrology*, 603, 127165.
779 <https://doi.org/10.1016/j.jhydrol.2021.127165>.

780 Singh, A., Chauhan, A., & Gaur, R. (2025), A comprehensive review on the synthesis, properties,
781 environmental impacts, and chemiluminescence applications of polystyrene (PS), *Discover*
782 *Chemistry*, 2(1), 47. <https://doi.org/10.1007/s44371-025-00125-y>.

783 Stoeckl, L., & Houben, G. (2012), Flow dynamics and age stratification of freshwater lenses:
784 Experiments and modeling, *Journal of Hydrology*, 458-459, 9-15.
785 <https://doi.org/10.1016/j.jhydrol.2012.05.070>.

786 Tang, Y., Lu, C., & Luo, J. (2022), An Analytical solution for groundwater lens pumping in a
787 three-dimensional rectangular island, *Journal of Hydrology*, 617, 128928.
788 <https://doi.org/10.1016/j.jhydrol.2022.128928>.

789 Tang, Y., Lu, C., & Luo, J. (2024), Optimizing groundwater pumping in small island groundwater
790 lenses: An analytical approach, *Journal of Hydrology*, 629, 130579.
791 <https://doi.org/10.1016/j.jhydrol.2023.130579>.

792 Tang, Y., Rathore, S., Lu, C., & Luo, J. (2020), Development of Groundwater Lens for Transient
793 Recharge in Strip Islands, *Journal of Hydrology*, 590, 125209.
794 <https://doi.org/10.1016/j.jhydrol.2020.125209>.

795 Tang, Y., Yan, M., Wang, X., Lu, C., & Luo, J. (2021), Experimental and modeling investigation of
796 pumping from a fresh groundwater lens in an idealized strip island, *Journal of Hydrology*,

797 602, 126734. <https://doi.org/10.1016/j.jhydrol.2021.126734>.

798 ten Hietbrink, S., Materić, D., Holzinger, R., Groeskamp, S., & Niemann, H. (2025), Nanoplastic
799 concentrations across the North Atlantic, *Nature*, 643(8071), 412-416.
800 <https://doi.org/10.1038/s41586-025-09218-1>.

801 Thompson, R. C., Courtene-Jones, W., Boucher, J., Pahl, S., Raubenheimer, K., & Koelmans, A. A.
802 (2024), Twenty years of microplastic pollution research—what have we learned?, *Science*,
803 386(6720), ead12746. <https://doi.org/10.1126/science.adl2746>.

804 van Genuchten, M.T. (1980), A Closed-form Equation for Predicting the Hydraulic Conductivity
805 of Unsaturated Soils. *Soil Science Society of America Journal*, 44: 892-898.
806 <https://doi.org/10.2136/sssaj1980.03615995004400050002x>.

807 Voss, C., & Provost, A. M. (2002), SUTRA: A model for 2D or 3D saturated-unsaturated,
808 variable-density ground-water flow with solute or energy transport, Report Rep. 2002-4231.
809 <https://doi.org/10.3133/wri024231>.

810 Waldschläger, K., & Schüttrumpf, H. (2020), Infiltration Behavior of Microplastic Particles with
811 Different Densities, Sizes, and Shapes—From Glass Spheres to Natural Sediments,
812 *Environmental Science & Technology*, 54(15), 9366-9373.
813 <https://doi.org/10.1021/acs.est.0c01722>.

814 Wang, R., Shu, L., Zhang, R., & Ling, Z. (2023), Determination of Exploitable Coefficient of
815 Coral Island Freshwater Lens Considering the Integrated Effects of Lens Growth and
816 Contraction, *Water*, 15(5), 890. <https://doi.org/10.3390/w15050890>.

817 Wang, X., Bolan, N., Tsang, D. C. W., Sarkar, B., Bradney, L., & Li, Y. (2021), A review of
818 microplastics aggregation in aquatic environment: Influence factors, analytical methods, and
819 environmental implications, *Journal of hazardous materials*, 402, 123496.
820 <https://doi.org/10.1016/j.jhazmat.2020.123496>.

821 Wang, Z., & Sedighi, M. (2023), Dispersion properties of nanoplastic spheres in granular media at
822 low Reynolds numbers, *Journal of Contaminant Hydrology*, 259, 104244.
823 <https://doi.org/10.1016/j.jconhyd.2023.104244>.

824 Werner, A. D., Jakovovic, D., & Simmons, C. T. (2009), Experimental observations of saltwater
825 up-coning, *Journal of Hydrology*, 373(1), 230-241.
826 <https://doi.org/10.1016/j.jhydrol.2009.05.004>.

827 White, I., & Falkland, T. (2010), Management of freshwater lenses on small Pacific islands,
828 *Hydrogeology Journal*, 18(1), 227-246. <https://doi.org/10.1007/s10040-009-0525-0>.

829 Yan, M., Lu, C., Werner, A. D., & Luo, J. (2021), Analytical, Experimental, and Numerical
830 Investigation of Partially Penetrating Barriers for Expanding Island Freshwater Lenses, *Water
831 Resources Research*, 57(3), e2020WR028386. <https://doi.org/10.1029/2020WR028386>.

832 Yang, J., Wang, Q., Heidbüchel, I., Xu, T., & Lu, C. (2025), Cut-off walls alter nitrogen loads and
833 fluxes in small islands, *Journal of Hydrology*, 647, 132266.
834 <https://doi.org/10.1016/j.jhydrol.2024.132266>.

835 Yao, Y., Andrews, C., Zheng, Y., He, X., Babovic, V., & Zheng, C. (2019), Development of Fresh
836 Groundwater Lens in Coastal Reclaimed Islands, *Journal of Hydrology*, 573, 365-375.
837 <https://doi.org/10.1016/j.jhydrol.2019.03.062>.

838 Yuan, C., Hu, L., Ren, Z., Xu, X., Gui, X., Gong, X., Wu, R., Sima, J., & Cao, X. (2024), Marine
839 Microplastics Enhance Release of Arsenic in Coastal Aquifer during Seawater Intrusion
840 Process, *Journal of Hazardous Materials*, 475, 134804.

841 <https://doi.org/10.1016/j.jhazmat.2024.134804>.
842 Zheng, T. (2014), Numerical Analysis of Modeling Concepts for Salt Precipitation and Porosity -
843 Permeability Evolution during Brine Evaporation.
844 Zheng, T., Meng, Y., Meng, X., Gao, S., Zhang, L., Zhang, B., Liu, T., & Luo, J. (2025), Influence
845 of time-space variability of rainfall infiltration recharge on fresh groundwater lens, Physics of
846 Fluids, 37(3), 036623. <https://doi.org/10.1063/5.0253940>.
847